

## Spin splitting and strain in epitaxial monolayer WSe<sub>2</sub> on graphene

H. Nakamura,<sup>1,\*</sup> A. Mohammed,<sup>1</sup> Ph. Rosenzweig,<sup>1</sup> K. Matsuda,<sup>1,2</sup> K. Nowakowski,<sup>1,3</sup> K. Küster,<sup>1</sup> P. Wochner,<sup>1</sup> S. Ibrahimkuty,<sup>1</sup> U. Wedig,<sup>1</sup> H. Hussain,<sup>4</sup> J. Rawle,<sup>4</sup> C. Nicklin,<sup>4</sup> B. Stuhlhofer,<sup>1</sup> G. Cristiani,<sup>1</sup> G. Logvenov,<sup>1</sup> H. Takagi,<sup>1,5,6</sup> and U. Starke<sup>1</sup>

<sup>1</sup>Max Planck Institute for Solid State Research, 70569 Stuttgart, Germany

<sup>2</sup>Department of Applied Chemistry, Nagoya University, Nagoya 464-8603, Japan

<sup>3</sup>MESA+ Institute for Nanotechnology, University of Twente, 7500AE Enschede, The Netherlands

<sup>4</sup>Diamond Light Source Ltd., Didcot, Oxfordshire OX11 0DE, United Kingdom

<sup>5</sup>Department of Physics, University of Tokyo, 113-0033 Tokyo, Japan

<sup>6</sup>Institute for Functional Matter and Quantum Technologies, University of Stuttgart, 70569 Stuttgart, Germany



(Received 19 August 2019; revised manuscript received 9 December 2019; accepted 10 March 2020; published 6 April 2020)

We present the electronic and structural properties of monolayer WSe<sub>2</sub> grown by pulsed-laser deposition on monolayer graphene (MLG) on SiC. The spin splitting in the WSe<sub>2</sub> valence band at  $\bar{K}$  was  $\Delta_{SO} = 0.469 \pm 0.008$  eV, as determined by angle-resolved photoemission spectroscopy. Synchrotron-based grazing-incidence in-plane x-ray diffraction (XRD) revealed the in-plane lattice constant of monolayer WSe<sub>2</sub> to be  $a_{WSe_2} = 3.2757 \pm 0.0008$  Å. This indicates a lattice compression of  $-0.19\%$  relative to bulk WSe<sub>2</sub>. By using the experimentally determined graphene lattice constant ( $a_{MLG} = 2.4575 \pm 0.0007$  Å), we found that a  $3 \times 3$  unit cell of the slightly compressed WSe<sub>2</sub> is perfectly commensurate with a  $4 \times 4$  graphene lattice with a mismatch below 0.03%, which could explain why the monolayer WSe<sub>2</sub> is compressed on MLG. From XRD and first-principles calculations, we conclude that the observed size of strain will affect  $\Delta_{SO}$  only on the order of a few meV. In addition, angle-resolved, ultraviolet, and x-ray photoelectron spectroscopies shed light on the band alignment between WSe<sub>2</sub> and MLG/SiC and indicate electron transfer from graphene to the WSe<sub>2</sub> monolayer. As further revealed by atomic force microscopy, the WSe<sub>2</sub> island size depends on the number of carbon layers on top of the SiC substrate. This suggests that the epitaxy of WSe<sub>2</sub> favors the weak van der Waals interactions with graphene, while it is perturbed by the influence of the SiC substrate and its carbon buffer layer.

DOI: [10.1103/PhysRevB.101.165103](https://doi.org/10.1103/PhysRevB.101.165103)

### I. INTRODUCTION

Two-dimensional (2D) transition-metal dichalcogenides (TMDs)  $MX_2$  ( $M = \text{Mo}$  or  $\text{W}$ ,  $X = \text{S}$ ,  $\text{Se}$ , or  $\text{Te}$ ) possess outstanding electronic, spin, and optical properties at thicknesses of a few layers and hold great promise for future optoelectronic and spintronic applications [1–6]. In the monolayer limit, the breaking of structural inversion symmetry gives rise to a large spin splitting in the top valence band located at the  $\bar{K}$  and  $\bar{K}'$  points of the surface Brillouin zone [7–9]. Due to time reversal symmetry, the  $\bar{K}$  and  $\bar{K}'$  valleys have opposite out-of-plane spin polarizations, and each valley is associated with optical selection rules of opposite chirality as well as opposite signs of Berry curvature [7]. This leads to the valley-contrasting physics of monolayer TMDs, such as optical valley polarization and the valley Hall effect [1,4].

Recent advances in the application of TMDs as a quantum light source are remarkable, especially for WSe<sub>2</sub> [10–15], where the spin-valley degree of freedom is found to be robust also in locally bound carriers [15].

The spin splitting in the valence band at  $\bar{K}$  is revealed directly by angle-resolved photoemission spectroscopy (ARPES) [16–33]. Spin-resolved ARPES confirmed an out-of-plane spin polarization that disappears for an even number of layers, consistent with the idea that inversion asymmetry is essential for the spin splitting [28]. As demonstrated by theory and experiment, WSe<sub>2</sub> has the largest spin splitting  $\Delta_{SO}$  among all TMDs of  $2H$  type [7,8,20,21,33]. *Le et al.* reported  $\Delta_{SO} = 513$  meV in monolayer WSe<sub>2</sub> exfoliated from a bulk crystal [20], while very recent work on an exfoliated monolayer WSe<sub>2</sub> reported  $\Delta_{SO} = 485$  meV [34]. *Zhang et al.* found  $\Delta_{SO} = 475$  meV in monolayer WSe<sub>2</sub> grown by molecular beam epitaxy (MBE) on bilayer graphene/SiC [21]. The discrepancy in  $\Delta_{SO}$  between the MBE-grown and earlier exfoliated monolayer has been attributed to potential strain in the epitaxial TMD layer [21]. However, an evaluation of such strain in monolayer WSe<sub>2</sub> using a precise structural probe, such as x-ray diffraction, has thus far been missing in any of the ARPES-based studies.

Besides inducing strain, the substrate beneath a TMD could have an effect on its electronic properties by affecting the

\*Present address: Department of Physics, University of Arkansas, Fayetteville, Arkansas 72701, USA; hnakamur@uark.edu

Published by the American Physical Society under the terms of the [Creative Commons Attribution 4.0 International license](https://creativecommons.org/licenses/by/4.0/). Further distribution of this work must maintain attribution to the author(s) and the published article's title, journal citation, and DOI. Open access publication funded by the Max Planck Society.

growth mode or via charge redistribution at the interface [35]. TMDs on graphene represent a prototypical van der Waals (vdW) heterostructure where charge transfer could critically influence the physical properties of the TMD [36]. In this regard, ARPES of the graphene  $\pi$  bands before and after the creation of a vdW heterostructure could provide direct evidence of charge transfer across the TMD/graphene interface, but no such experiment has yet been reported. Alternatively, the charge transfer can be indirectly assessed from the position of the valence band maximum of the TMD  $E_K$  with respect to the Fermi level  $E_F$ . In  $WS_2$  grown by chemical vapor deposition on epitaxial monolayer graphene on SiC, Forti *et al.* found  $E_K = -1.84$  eV [30]. Taking into account a band gap  $E_G$  of 2.1 eV for pristine monolayer  $WS_2$ , where  $E_F$  is assumed to lie midgap, this corresponds to a significant downshift of  $\sim 0.8$  eV of the  $WS_2$  bands. This, in turn, indicates electron transfer to  $WS_2$  across the interface. For MBE-grown  $WSe_2$  on epitaxial bilayer graphene, ARPES and scanning tunneling spectroscopy (STS) yielded  $E_K \sim -1.1$  eV [21]. Considering a band gap of 1.95 eV as determined by STS, this also suggests a small downshift ( $\sim 100$  meV) of the  $WSe_2$  bands, consistent with an electron transfer to the TMD layer. On the other hand, ARPES of monolayer  $WSe_2$  transferred to cleaved graphite yielded  $E_K = -0.7$  eV [33]. Assuming the same band gap  $E_G$ , this corresponds to  $E_F$  residing closer to the valence band and thus indicates a hole transfer to  $WSe_2$ . However, we note that the above results are only indirect indications of charge transfer because the position of the Fermi level can depend on the way the respective heterostructure was prepared. To unambiguously resolve the issue of charge transfer across the TMD/graphene interface, a comparison of ARPES measurements performed both before and after the creation of the vdW heterostructure could be highly useful.

In this paper, we clarify the electronic structure of monolayer  $WSe_2$  grown by pulsed-laser deposition on epitaxial monolayer graphene on SiC (MLG/SiC). In particular, we address the issue of a potential strain effect on the spin splitting  $\Delta_{SO}$  by using ARPES and grazing-incidence x-ray diffraction (GIXRD) data, supported by an analysis based on first-principles calculations. The electron transfer from graphene to  $WSe_2$  is revealed by comparing ARPES of the graphene  $\pi$  bands before and after the  $WSe_2$  deposition. Ultraviolet and x-ray photoelectron spectroscopies (UPS and XPS), which are also conducted before and after the  $WSe_2$  growth, shed light on the band alignment between monolayer  $WSe_2$  and graphene. Atomic force microscopy (AFM) further reveals a significant impact of the substrate morphology on the  $WSe_2$  island size.

## II. EXPERIMENT AND THEORY

Monolayer graphene on SiC was grown using the well-established recipe of sublimation growth at elevated temperatures in an argon atmosphere [37,38]. Note that, on SiC, the graphene monolayer resides on top of a  $(6\sqrt{3} \times 6\sqrt{3})R30^\circ$ -reconstructed carbon buffer layer (zerolayer graphene, ZLG) that is covalently bound to the SiC substrate [39].

$WSe_2$  films were grown on the thus prepared MLG/SiC substrates via hybrid-pulsed-laser deposition (hPLD) in ultrahigh vacuum (UHV) [40]. This recently developed,

bottom-up technique utilizes a pulsed laser to ablate transition-metal targets, supported by chalcogen vapor supplied from an effusion cell, thus combining PLD and MBE. Pure tungsten (99.99%) was ablated using a pulsed KrF excimer laser (248 nm) with a repetition rate of 10 Hz, while pure selenium (99.999%) was evaporated from a Knudsen cell at a flux rate of around  $1.5 \text{ \AA/s}$  as monitored by a quartz crystal microbalance. The deposition was carried out at  $450^\circ\text{C}$  for 3 h, followed by two-step annealing at  $640^\circ\text{C}$  and  $400^\circ\text{C}$  for 1 h each. Further details on hPLD can be found elsewhere [40].

GIXRD measurements were carried out at the I07 beamline of the Diamond Light Source [41], with a photon energy of 12 keV (wavelength of  $1.0332 \text{ \AA}$ ) and a Pilatus 100K 2D detector (DECTRIS). The incident angle  $\alpha \sim 0.2^\circ$  of the x rays was chosen according to the critical angle of the samples, which were kept in a helium atmosphere during the measurements. Topographic AFM images were acquired with a Bruker microscope in peak force tapping mode.

For photoelectron spectroscopy and low-energy electron diffraction (LEED), the freshly prepared samples were capped with a 10-nm-thick selenium layer at room temperature and transported through air into a different UHV facility, where the capping layer was removed by heating to  $300^\circ\text{C}$ . ARPES and UPS measurements were performed using monochromatized He I  $\alpha$  (21.22 eV) and He II  $\alpha$  (40.81 eV) photons and a 2D hemispherical analyzer equipped with a CCD detector (SPECS Phoibos 150). The energy resolution of the ARPES analyzer was 60 or 90 meV at a pass energy of 20 or 30 eV, respectively, as measured from the Fermi edge of gold at room temperature. However, the peak positions could be determined with much better accuracy as detailed in the Supplemental Material [42]. XPS was carried out using nonmonochromatized Mg  $K\alpha$  (1253.6 eV) radiation. All the measurements took place at room temperature.

First-principles calculations were performed using density functional theory as implemented in WIEN2K [43] and ADF-BAND [44,45]. The generalized gradient approximation as parameterized by Perdew, Burke, and Ernzerhof [46] was used to describe the exchange-correlation functional. The spin-orbit coupling is included in a second variational procedure (WIEN2K) or in the original basis set (ADF-BAND). We used a  $k$ -point mesh of  $16 \times 16 \times 1$  and adopted a slab geometry with a 30- $\text{\AA}$  gap between adjacent layers to suppress the interlayer interaction.

## III. RESULTS AND DISCUSSION

### A. Electronic structure and strain

The vertical structure of the  $WSe_2$ /MLG heterostack is schematically shown in Fig. 1(a). Figures 1(c) and 1(d) show the LEED patterns obtained before and after the growth of monolayer  $WSe_2$  on MLG/SiC with a coverage of approximately 50%, demonstrating the preferred epitaxial relationship between  $WSe_2$  and graphene ( $WSe_2$   $[10\bar{1}0] \parallel$  graphene  $[10\bar{1}0]$ ). This epitaxial relationship of the vdW heterostructure results in a reciprocal space alignment, as shown in Fig. 1(b). The ARPES intensity map recorded along the  $\overline{\Gamma K}$  direction of  $WSe_2$  and graphene is shown in Fig. 1(h). The valence

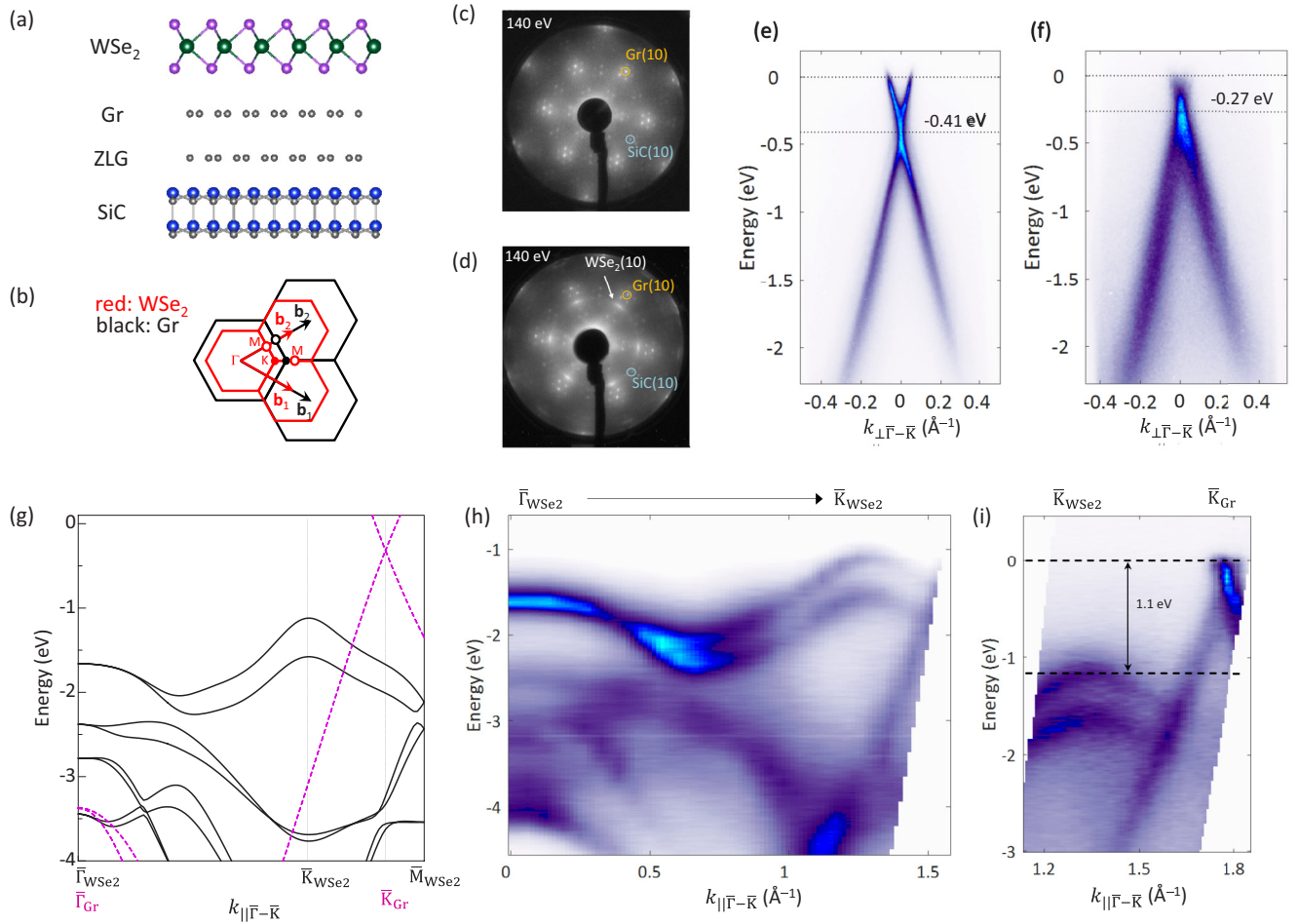


FIG. 1. ARPES of monolayer WSe<sub>2</sub>. (a) Schematic side view of the WSe<sub>2</sub>/MLG van der Waals heterostructure. (b) Reciprocal space alignment for WSe<sub>2</sub> and graphene. LEED images (c) before and (d) after the growth of WSe<sub>2</sub>. ARPES dispersion of the Dirac bands of graphene measured perpendicular to graphene's  $\bar{\Gamma}\bar{K}$  direction (e) before and (f) after the growth of WSe<sub>2</sub>. (g) Band diagram of WSe<sub>2</sub> (solid lines) and graphene (dashed lines) obtained from first-principles calculation. (h) ARPES data taken along the  $\bar{\Gamma}\bar{K}$  direction of WSe<sub>2</sub>. (i) ARPES taken at a region including the Dirac point of graphene and the top of the WSe<sub>2</sub> valence bands.

bands of monolayer WSe<sub>2</sub> are resolved with excellent quality, essentially consistent with the result of the first-principles calculation [see Fig. 1(g)]. As expected from the reciprocal space alignment, the graphene  $\pi$  bands with their characteristic linear dispersion in the vicinity of the Fermi level  $E_F$  also appear at higher parallel momenta  $k_{\parallel}$  [see Figs. 1(h) and 1(i)]. Note that the  $\pi$  bands are shifted in energy before and after the WSe<sub>2</sub> deposition, as revealed by the corresponding energy-momentum cuts recorded at the graphene  $\bar{K}$  point perpendicular to the  $\bar{\Gamma}\bar{K}$  direction [see Figs. 1(e) and 1(f)]. Before the WSe<sub>2</sub> deposition, the Dirac point is found 0.41 eV below  $E_F$ , reflecting the  $n$ -type doping of epitaxial graphene on SiC [39]. After the growth of WSe<sub>2</sub> on top of graphene, the Dirac point shifts to 0.27 eV below  $E_F$ . This upshift of 140 meV indicates electron transfer from graphene to the TMD monolayer which will be further discussed in Sec. III B.

The large spin splitting  $\Delta_{SO}$  arising in the topmost WSe<sub>2</sub> valence band at  $\bar{K}$  due to the breaking of inversion symmetry in monolayer WSe<sub>2</sub> is clearly resolved in the ARPES data [see Figs. 1(h), 1(i), 2(a), and 2(b)]. To quantify this splitting, an energy distribution curve (EDC) was extracted at the  $\bar{K}$  point of WSe<sub>2</sub>, as indicated by the dashed black line in Fig. 2(a).

By fitting this EDC with two pseudo-Voigt curves as shown in Fig. 2(b), we obtain  $\Delta_{SO} = 0.469 \pm 0.008$  eV. Details of the EDC analysis can be found in the Supplemental Material [42]. This value is appreciably smaller than the 513 meV observed in monolayer WSe<sub>2</sub> exfoliated from a bulk crystal [20] but close to a more recent result (485 meV) [34] as well as MBE-grown WSe<sub>2</sub> (475 meV) [21]. While it is tempting to relate this difference to strain resulting from the epitaxial TMD growth, we will show in the following that the influence of strain on  $\Delta_{SO}$  is actually negligible for WSe<sub>2</sub> on graphene.

We first focus on the results obtained from synchrotron-based GIXRD [40]. Utilizing an x-ray beam that propagates parallel to the sample surface at a critical angle of incidence  $\alpha \sim 0.2^\circ$  [see Fig. 3(a)], this technique probes the in-plane structure of the WSe<sub>2</sub> film [see Fig. 3(b)]. The in-plane reciprocal space map shown in Fig. 3(c) clearly captures diffraction from monolayer WSe<sub>2</sub>. We find WSe<sub>2</sub> [1010]  $\parallel$  graphene [10 $\bar{1}$ 0], fully consistent with LEED [see Fig. 1(d)]. The weak ringlike elongation of the WSe<sub>2</sub> diffraction in the reciprocal space map reflects a large crystalline mosaic of monolayer WSe<sub>2</sub> islands with different rotation angles around the surface normal. The wide-angle ( $\pm 100^\circ$ ) rocking  $\theta$  scan

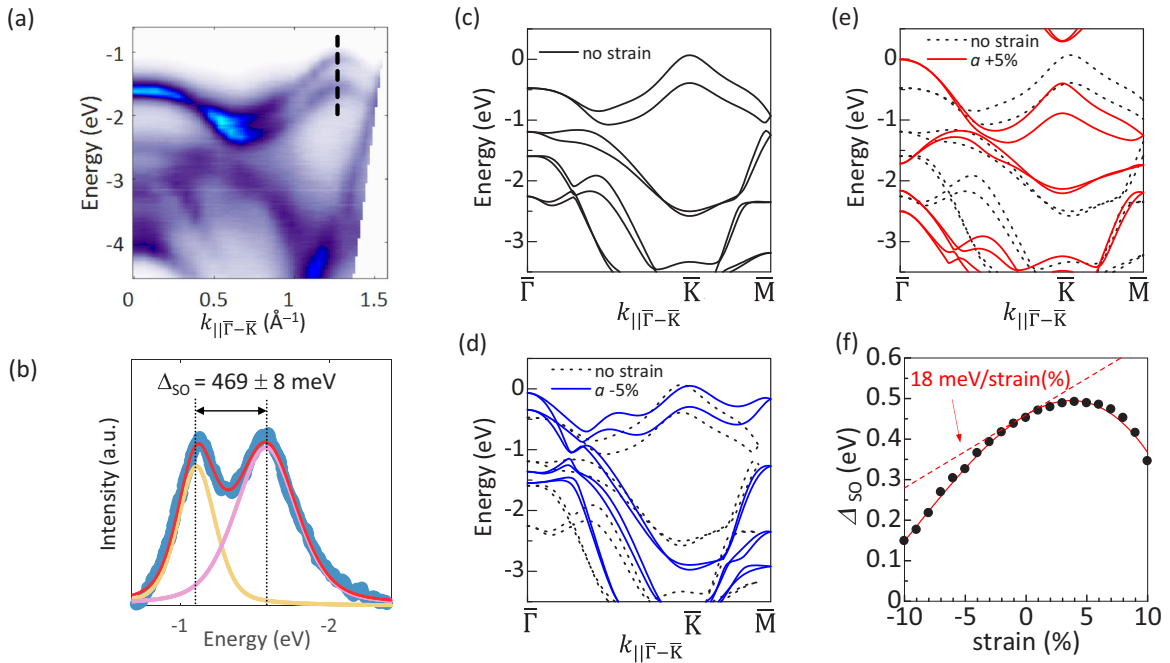


FIG. 2. (a) Raw ARPES data displaying the large spin splitting in the topmost WSe<sub>2</sub> valence band at  $\bar{K}$  (dashed black line). (b) EDC extracted at  $\bar{K}$  of WSe<sub>2</sub> (blue dots) together with the fit (red curve) that consists of two pseudo-Voigt functions (light orange and light purple curves). Band structures of WSe<sub>2</sub> obtained from a first-principles calculation assuming (c) no strain, (d) 5% compressive strain (in plane), and (e) 5% tensile strain (in plane). (f) The spin splitting  $\Delta_{SO}$  as a function of in-plane strain as extracted from the first-principles calculations.

for the WSe<sub>2</sub> (110) peak exhibits the expected periodicity of 60°, as shown in Fig. 3(e). To evaluate the potential strain in the epitaxial TMD film, the in-plane lattice constant  $a$  of WSe<sub>2</sub> was extracted from the  $\delta$ - $\theta$  scans shown in Fig. 3(d). We find  $a = 3.2757 \pm 0.0008$  Å, which indicates a small compression of  $-0.19\%$  with respect to the bulk reference value ( $a = 3.282 \pm 0.001$  Å [47]). Details on the extraction of the lattice constant and its error are shown in the Supplemental Material [42]. The lattice constant of MLG directly

beneath WSe<sub>2</sub> is determined to be  $a_{MLG} = 2.4575 \pm 0.0007$  Å from the same  $\delta$ - $\theta$  scans. Using these values, we deduce that on MLG/SiC, a  $3 \times 3$  unit cell of the compressed WSe<sub>2</sub> is perfectly commensurate with a  $4 \times 4$  graphene lattice, with an experimentally determined mismatch below 0.03%. This could explain why monolayer WSe<sub>2</sub> is compressed on MLG.

We now turn to the result of the first-principles calculations to examine the role of strain. Figures 2(c)–2(f) show how

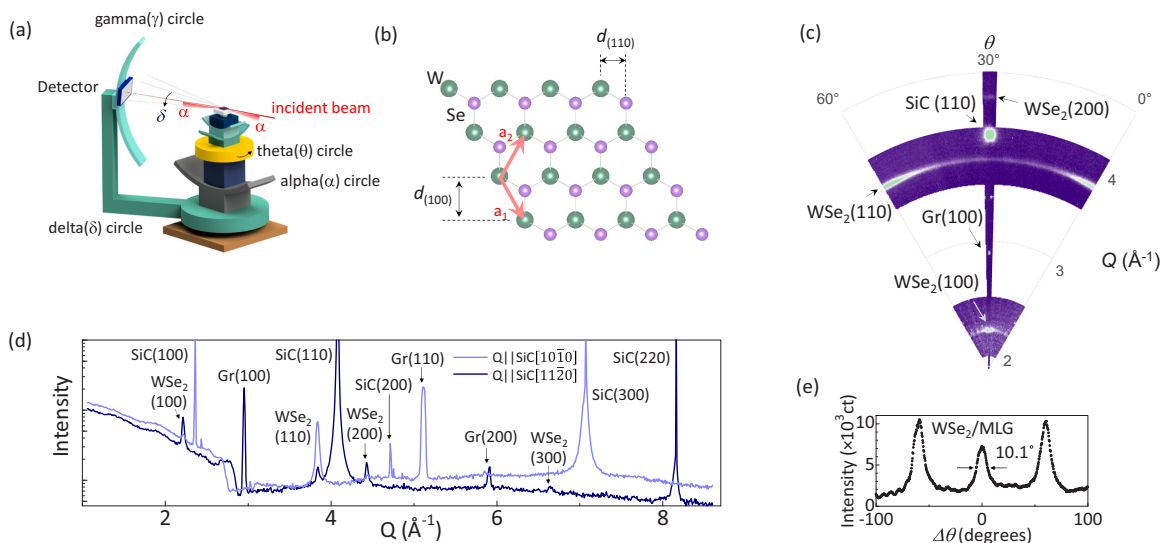


FIG. 3. Grazing incidence in-plane x-ray diffraction (GIXRD) of monolayer WSe<sub>2</sub>/MLG/SiC. (a) Schematic diagram of the GIXRD geometry.  $\alpha \sim 0.2^\circ$  is the incidence angle of the x-ray beam. (b) In-plane structure of WSe<sub>2</sub>. The two primary in-plane lattice spacings are highlighted. (c) Reciprocal space map for WSe<sub>2</sub> on MLG. (d) In-plane  $\delta$ - $\theta$  scans along two distinct crystallographic directions ( $\mathbf{Q} \parallel \text{SiC}[10\bar{1}0]$  and  $\text{SiC}[11\bar{2}0]$ ). (e) Wide-angle rocking  $\theta$  scan of the WSe<sub>2</sub> (110) Bragg reflection.

a compressive or tensile strain modifies the valence band structure of monolayer WSe<sub>2</sub>. In the respective calculations, the in-plane lattice constant was changed proportionally to include strain while keeping the unit cell volume constant. Qualitatively, our calculations indicate that compressive strain reduces the value of  $\Delta_{SO}$  [see Fig. 2(f)], which is in accordance with previous first-principles results [20]. We find  $\Delta_{SO} = 452$  (475) meV using WIEN2K (ADF-BAND) for “zero strain,” i.e., when we set the lattice constant of monolayer WSe<sub>2</sub> identical to the bulk value. By introducing strain, the inferred change in  $\Delta_{SO}$  is +18 (−18) meV per 1% of tensile (compressive) strain, as shown in Fig. 2(f). This holds for moderately strained WSe<sub>2</sub> (as is the case in the present experiment), while the general dependence of  $\Delta_{SO}$  on strain is clearly nonlinear. Using our experimentally determined value of the lattice compression of WSe<sub>2</sub> on graphene (−0.19%), the change in  $\Delta_{SO}$  that could arise from compressive strain is −3.4 meV.

A subtle issue in the approach we used to estimate strain is that we actually do not know the lattice constant of a freestanding monolayer WSe<sub>2</sub>. Even without substrate effects, such freestanding monolayer may not have the same lattice constant as its bulk counterpart. To examine this, we performed additional first-principles calculations for bulk and monolayer WSe<sub>2</sub> with structural optimization [42]. The theoretical results show that the lattice constant of monolayer WSe<sub>2</sub> converges to a value almost identical to that of the bulk WSe<sub>2</sub> (expanded by only about +0.03%). This means that the experimentally observed compression (−0.19%) can, indeed, be associated with strain in monolayer WSe<sub>2</sub> as discussed above.

A very recent ARPES study of exfoliated WSe<sub>2</sub> by Nguyen *et al.* [34] showed that (i)  $\Delta_{SO} = 0.485 \pm 0.01$  eV for a monolayer, in good agreement with the value observed in our experiments, and (ii)  $\Delta_{SO} = 0.501 \pm 0.01$  eV for bilayer WSe<sub>2</sub>. The latter value is actually quite close to that of exfoliated monolayer WSe<sub>2</sub> reported in an earlier study [20]. Thus, the large spin splitting of Ref. [20] might originate due to some inclusion of bilayer WSe<sub>2</sub> in the exfoliated monolayer.

## B. Band alignment and charge transfer

The sample work function  $\phi$  can be measured using UPS. From the secondary cutoffs of the respective spectra shown in Fig. 4(a), we infer  $\phi = 4.13$  and 4.40 eV ( $\pm 0.04$  eV) before and after the growth of WSe<sub>2</sub>, respectively. In combination with the ARPES results of Sec. III A, we derive the band alignment of the WSe<sub>2</sub>/MLG heterostructure as sketched in Fig. 4(c). In quasifreestanding graphene, the bulk polarization of the SiC substrate induces an upward band bending, which would result in *p* doping of the surface when terminated by a clean interface [48]. Yet with the presence of the carbon buffer layer (ZLG) this is overcompensated by donor states at the graphene/SiC interface, resulting in the *n*-type character of epitaxial MLG/SiC [49] with its Dirac point residing 0.41 eV below  $E_F$  [see Fig. 1(e)]. As discussed in Sec. III A, the Dirac point shifts up by 0.14 eV to 0.27 eV below  $E_F$  upon WSe<sub>2</sub> growth [see Fig. 1(f)]. To our knowledge, such a shift of the graphene  $\pi$  bands upon TMD growth on top was not reported previously. There are two possible mechanisms to explain this

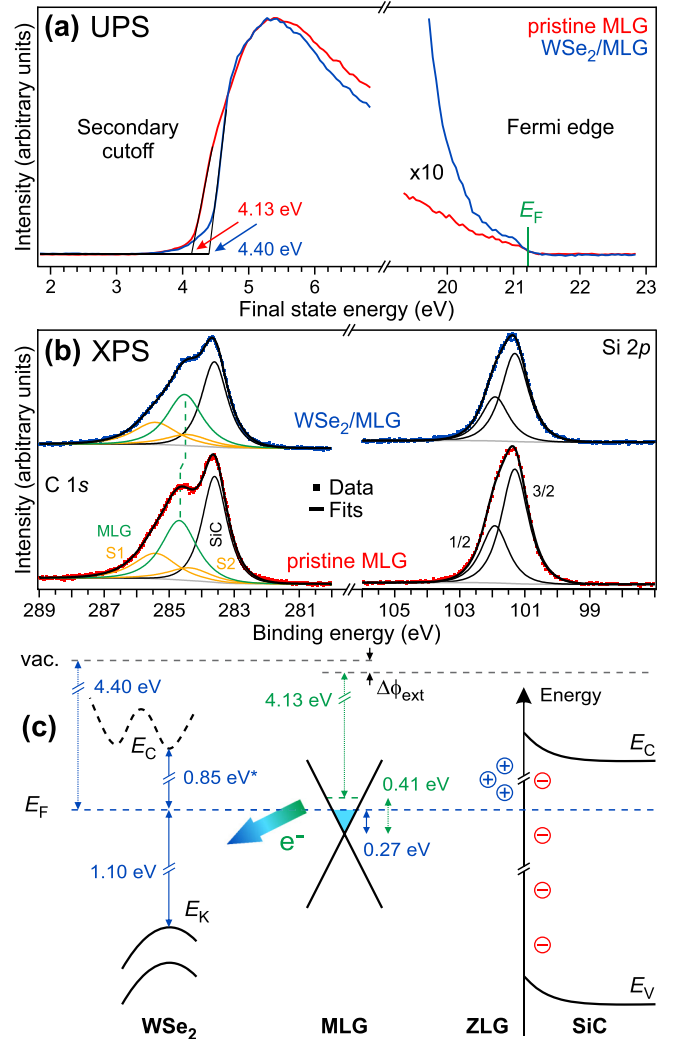


FIG. 4. (a) UPS spectra obtained from pristine MLG (red) and WSe<sub>2</sub>/MLG (blue). On the final-state-energy axis, the respective sample work function can directly be read off from the secondary cutoff (red and blue arrows). (b) XPS core level spectra of C 1s and Si 2p. The shift of the MLG peak (green curve) to lower binding energies upon WSe<sub>2</sub> growth is consistent with the observed charge transfer from MLG onto WSe<sub>2</sub>. All other components are found unshifted, indicating that the band bending at the graphene/SiC interface is unperturbed by the WSe<sub>2</sub> growth. (c) Schematic band alignment of the WSe<sub>2</sub>/MLG heterostructure as obtained from photoelectron spectroscopy (not drawn to scale). The polarity contribution to the upward band bending at the ZLG/SiC interface (red circles) is partially compensated by donor states (blue circles). Electron transfer from graphene onto WSe<sub>2</sub> is indicated by the filled arrow. The Fermi energy before (after) the WSe<sub>2</sub> growth is shown by the green (blue) dashed lines. The additional contribution  $\Delta\phi_{\text{ext}}$  to the work function change results from an upshift of the vacuum level due the change in surface termination from MLG to WSe<sub>2</sub>.

observation. First, electron transfer from graphene to WSe<sub>2</sub> could shift the graphene bands upwards. Second, if the donor states at the graphene/SiC interface are partially compensated during the TMD growth (e.g., via chemical reaction with the Se vapor), the amount of *n*-type doping of graphene could change. In the latter case, modified donor states should

influence the band bending at the graphene/SiC interface, which can be detected via a shift of the SiC core levels.

The fitted XPS core level spectra of C  $1s$  and Si  $2p$  are shown in Fig. 4(b). The C  $1s$  fits consist of four components representing bulk SiC, MLG, and the carbon buffer layer with its partial bonding to SiC (S1 and S2) [39]. The Si  $2p$  spectra can reasonably well be fitted by one spin-orbit split doublet ( $j = 3/2$  and  $1/2$  with an area ratio of 2:1). We find that the SiC peaks are unshifted in energy after the growth of WSe<sub>2</sub>, indicating that the band bending at the interface remains unchanged. From this, we can exclude the possibility that the reduced  $n$ -type doping of graphene results from a modification of the interfacial donor states during TMD growth. Upon WSe<sub>2</sub> growth the C  $1s$  MLG component shifts by  $0.16 \pm 0.02$  eV to lower binding energies while S1 and S2 retain their positions. This core level shift of MLG is quantitatively in line with the upshift of the Dirac point observed in ARPES and further supports the scenario of electron transfer from MLG to WSe<sub>2</sub>. The work function increases by the charge transfer, and we ascribe the remaining increase of  $0.27 - 0.14 = 0.13$  eV to an extrinsic upshift  $\Delta\phi_{\text{ext}}$  of the vacuum level due to the change in surface termination from MLG to WSe<sub>2</sub> [see Fig. 4(c)].

The valence band maximum  $E_K$  of WSe<sub>2</sub> is found  $\sim 1.1$  eV below  $E_F$  in our ARPES measurements [see Fig. 1(i)], which matches very well with the results obtained from MBE-grown epitaxial WSe<sub>2</sub> on bilayer graphene [21]. By assuming a band gap of 1.95 eV as previously determined by STS [21], we estimate that the conduction band minimum  $E_C$  is located  $\sim 0.85$  eV above  $E_F$ . As such, the Fermi level in WSe<sub>2</sub> resides closer to the conduction band minimum than to the valence band maximum. We finally note that a finite density of in-gap states can be expected in our epitaxial WSe<sub>2</sub> films, stabilizing the position of  $E_F$  inside the band gap after the electron transfer from graphene.

### C. Morphology of monolayer WSe<sub>2</sub>

The morphology of monolayer WSe<sub>2</sub> was measured by AFM. The unique feature of the hPLD-grown films was a high spatial uniformity with relatively small island sizes. Larger-scale AFM images show a high density of nucleation sites distributed uniformly over the surface [see Fig. 5(a)]. The epitaxial graphene substrate had minor inhomogeneities on the surface resulting from the fabrication process: small areas of bilayer graphene (BLG) close to the step edges as well as exposed buffer layer (ZLG) regions within the flat MLG terraces. Notably, WSe<sub>2</sub> islands were indiscernible on ZLG by AFM [see Fig. 5(b)]. On the other hand, islands on BLG tended to be larger (frequently approaching  $\sim 100$  nm) than on MLG [see Fig. 5(b)]. The different WSe<sub>2</sub> island sizes throughout the epitaxial graphene substrate are likely related to the distinct chemical nature and morphology of BLG, MLG, and ZLG. During the TMD growth process, the migration of species could be severely limited on ZLG due to its covalent bonding to SiC and the resultant buckled surface [50], in contrast to the weak interaction on complete vdW layers (MLG and BLG). Note that BLG regions may have an even smoother surface than MLG regions due to the remoteness to the covalent bonds between ZLG and the SiC

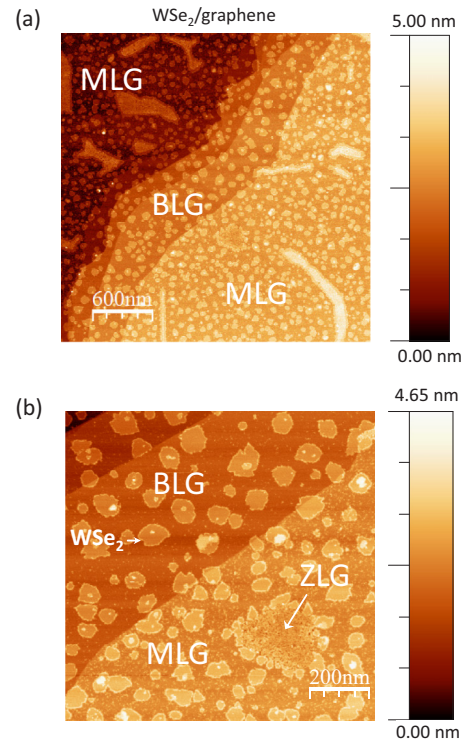


FIG. 5. Topographic AFM images of epitaxial WSe<sub>2</sub> on MLG/SiC. Lateral dimensions are (a)  $3 \times 3 \mu\text{m}^2$  and (b)  $1 \times 1 \mu\text{m}^2$ .

substrate. Thus, our results clearly highlight the advantage of a chemically inert and smooth vdW surface in obtaining larger WSe<sub>2</sub> domains during the epitaxial growth.

## IV. SUMMARY AND CONCLUSIONS

In summary, we have grown monolayer WSe<sub>2</sub> on top of epitaxial monolayer graphene on SiC by hybrid-pulsed-laser deposition and examined its electronic and structural properties. A spin splitting of  $\Delta_{SO} = 0.469 \pm 0.008$  eV is found for the topmost WSe<sub>2</sub> valence band at  $\bar{K}$ . The in-plane lattice constant of WSe<sub>2</sub> was determined by grazing incidence x-ray diffraction, revealing a small compression ( $-0.19\%$ ) of the epitaxial monolayer WSe<sub>2</sub> film with respect to its bulk counterpart. Supplementing these data with first-principles calculations, we clarify that strain influences  $\Delta_{SO}$  only on the order of a few meV in our epitaxial film. This makes our study a valuable reference in which both ARPES and XRD have been performed with high accuracies. Furthermore, the overall band alignment between WSe<sub>2</sub> and graphene was clarified. The electron transfer from graphene to WSe<sub>2</sub> becomes apparent from an upshift of the Dirac point of graphene towards the Fermi level after the growth of the TMD monolayer. The varying WSe<sub>2</sub> island sizes on substrate areas covered by graphene layers of different thicknesses suggest the importance of atomically smooth, weakly interacting van der Waals surfaces for monolayer TMD epitaxy. Our results provide high-quality data on both electronic and structural properties of monolayer WSe<sub>2</sub> and shed light on potential substrate influences in bottom-up TMD growth.

## ACKNOWLEDGMENTS

We are grateful to D. Huang and D. Weber for discussions and a critical reading of the manuscript. We thank S. Prill-Drimmer, K. Pflaum, M. Dueller, and F. Adams for technical

support. We acknowledge the Diamond Light Source for time on Beamline I07 under Proposal SI18887 and the Calipso program for the financial support. This work was supported by the Alexander von Humboldt Foundation.

- [1] K. F. Mak and J. Shan, *Nat. Photonics* **10**, 216 (2016).
- [2] P. Rivera, H. Yu, K. L. Seyler, N. P. Wilson, W. Yao, and X. Xu, *Nat. Nanotechnol.* **13**, 1004 (2018).
- [3] G. Wang, A. Chernikov, M. M. Glazov, T. F. Heinz, X. Marie, T. Amand, and B. Urbaszek, *Rev. Mod. Phys.* **90**, 021001 (2018).
- [4] K. F. Mak, D. Xiao, and J. Shan, *Nat. Photonics* **12**, 451 (2018).
- [5] Q. H. Wang, K. K. Zadeh, A. Kis, J. N. Coleman, and M. S. Strano, *Nat. Nanotechnol.* **7**, 699 (2012).
- [6] K. S. Novoselov, A. Mishchenko, A. Carvalho, and A. H. Castro Neto, *Science* **353**, aac9439 (2016).
- [7] D. Xiao, G. B. Liu, W. Feng, X. Xu, and W. Yao, *Phys. Rev. Lett.* **108**, 196802 (2012).
- [8] Z. Y. Zhu, Y. C. Cheng, and U. Schwingenschlögl, *Phys. Rev. B* **84**, 153402 (2011).
- [9] H. Yuan, M. S. Bahramy, K. Morimoto, S. Wu, K. Nomura, B. J. Yang, H. Shimotani, R. Suzuki, M. Toh, C. Kloc, X. Xu, R. Arita, N. Nagaosa, and Y. Iwasa, *Nat. Phys.* **9**, 563 (2013).
- [10] A. Srivastava, M. Sidler, A. V. Allain, D. S. Lembke, A. Kis, and A. Imamoglu, *Nat. Nanotechnol.* **10**, 491 (2015).
- [11] Y. M. He, G. Clark, J. R. Schaibley, Y. He, M. C. Chen, Y. J. Wei, X. Ding, Q. Zhang, W. Yao, X. Xu, C. Y. Lu, and J. W. Pan, *Nat. Nanotechnol.* **10**, 497 (2015).
- [12] M. Koperski, K. Nogajewski, A. Arora, V. Cherkez, P. Mallet, J.-Y. Veuillen, J. Marcus, P. Kossacki, and M. Potemski, *Nat. Nanotechnol.* **10**, 503 (2015).
- [13] C. Chakraborty, L. Kinnischtzke, K. M. Goodfellow, R. Beams, and A. N. Vamivakas, *Nat. Nanotechnol.* **10**, 507 (2015).
- [14] Y. Luo, G. D. Shepard, J. V. Ardelean, D. A. Rhodes, B. Kim, K. Barmak, J. C. Hone, and S. Strauf, *Nat. Nanotechnol.* **13**, 1137 (2018).
- [15] X. Lu, X. Chen, S. Dubey, Q. Yao, W. Li, X. Wang, Q. Xiong, and A. Srivastava, *Nat. Nanotechnol.* **14**, 426 (2019).
- [16] Y. Zhang, T. R. Chang, B. Zhou, Y. T. Cui, H. Yan, Z. Liu, F. Schmitt, J. Lee, R. Moore, Y. Chen, H. Lin, H. T. Jeng, S. K. Mo, Z. Hussain, A. Bansil, and Z. X. Shen, *Nat. Nanotechnol.* **9**, 111 (2013).
- [17] M. H. Chiu, M. Y. Li, W. Zhang, W. T. Hsu, W. H. Chang, M. Terrones, H. Terrones, and L. J. Li, *ACS Nano* **8**, 9649 (2014).
- [18] T. Eknapakul, P. D. C. King, M. Asakawa, P. Buaphet, R. H. He, S. K. Mo, H. Takagi, K. M. Shen, F. Baumberger, T. Sasagawa, S. Jungthawan, and W. Meevasana, *Nano Lett.* **14**, 1312 (2014).
- [19] J. M. Riley, F. Mazzola, M. Dendzik, M. Michiardi, T. Takayama, L. Bawden, C. Granerød, M. Leandersson, T. Balasubramanian, M. Hoesch, T. K. Kim, H. Takagi, W. Meevasana, Ph. Hofmann, M. S. Bahramy, J. W. Wells, and P. D. C. King, *Nat. Phys.* **10**, 835 (2014).
- [20] D. Le, A. Barinov, E. Preciado, M. Isarraraz, I. Tanabe, T. Komesu, C. Troha, L. Bartels, T. S. Rahman, and P. A. Dowben, *J. Phys.: Condens. Mater.* **27**, 182201 (2015).
- [21] Y. Zhang, M. M. Ugeda, C. Jin, S. F. Shi, A. J. Bradley, A. Martín-Recio, H. Ryu, J. Kim, S. Tang, Y. Kim, B. Zhou, C. Hwang, Y. Chen, F. Wang, M. F. Crommie, Z. Hussain, Z. X. Shen, and S. K. Mo, *Nano Lett.* **16**, 2485 (2016).
- [22] K. E. Aretouli, P. Tsipas, D. Tsoutsou, J. Marquez-Velasco, E. Xenogiannopoulou, S. A. Giamini, E. Vassalou, N. Kelaidis, and A. Dimoulas, *Appl. Phys. Lett.* **106**, 143105 (2015).
- [23] H. C. Diaz, J. Avila, C. Chen, R. Addou, M. C. Asensio, and M. Batzill, *Nano Lett.* **15**, 1135 (2015).
- [24] D. W. Latzke, W. Zhang, A. Suslu, T. R. Chang, H. Lin, H. T. Jeng, S. Tongay, J. Wu, A. Bansil, and A. Lanzara, *Phys. Rev. B* **91**, 235202 (2015).
- [25] J. M. Riley, W. Meevasana, L. Bawden, M. Asakawa, T. Takayama, T. Eknapakul, T. K. Kim, M. Hoesch, S. K. Mo, H. Takagi, T. Sasagawa, M. S. Bahramy, and P. D. C. King, *Nat. Nanotechnol.* **10**, 1043 (2015).
- [26] K. Sugawara, T. Sato, Y. Tanaka, S. Souma, and T. Takahashi, *Appl. Phys. Lett.* **107**, 071601 (2015).
- [27] K. E. Aretouli, D. Tsoutsou, P. Tsipas, J. Marquez-Velasco, S. A. Giamini, N. Kelaidis, V. Psycharis, and A. Dimoulas, *ACS Appl. Mater. Interfaces* **8**, 23222 (2016).
- [28] S. K. Mo, C. Hwang, Y. Zhang, M. Fanciulli, S. Muff, J. H. Dil, Z. X. Shen, and Z. Hussain, *J. Phys.: Condens. Matter* **28**, 454001 (2016).
- [29] Z. Ben Aziza, D. Pierucci, H. Henck, M. G. Silly, C. David, M. Yoon, F. Sirotti, K. Xiao, M. Eddrief, J. C. Girard, and A. Ouerghi, *Phys. Rev. B* **96**, 035407 (2017).
- [30] S. Forti, A. Rossi, H. Büch, T. Cavallucci, F. Bisio, A. Sala, T. O. Mentş, A. Locatelli, M. Magnozzi, M. Canepa, K. Müller, S. Link, U. Starke, V. Tozzini, and C. Colletti, *Nanoscale* **9**, 16412 (2017).
- [31] H. Henck, Z. Ben Aziza, O. Zill, D. Pierucci, C. H. Naylor, M. G. Silly, N. Gogneau, F. Oehler, S. Collin, J. Brault, F. Sirotti, F. Bertran, P. Le Fèvre, S. Berciaud, A. T. C. Johnson, E. Lhuillier, J. E. Rault, and A. Ouerghi, *Phys. Rev. B* **96**, 115312 (2017).
- [32] S. Agnoli, A. Ambrosetti, T. O. Mentş, A. Sala, A. Locatelli, P. L. Silvestrelli, M. Cattelan, S. Eichfeld, D. D. Deng, J. A. Robinson, J. Avila, C. Chen, and M. C. Asensio, *ACS Appl. Nano Mater.* **1**, 1131 (2018).
- [33] N. R. Wilson, P. V. Nguyen, K. Seyler, P. Rivera, A. J. Marsden, Z. P. L. Laker, G. C. Constantinescu, V. Kandyba, A. Barinov, N. D. M. Hine, X. Xu, and D. H. Cobden, *Sci. Adv.* **3**, e1601832 (2017).
- [34] P. V. Nguyen, N. C. Teutsch, N. P. Wilson, J. Kahn, X. Xia, A. J. Graham, V. Kandyba, A. Giampietry, A. Barinov, G. C. Constantinescu, N. Yeung, N. D. M. Hine, X. Xu, D. H. Cobden, and N. R. Wilson, *Nature (London)* **572**, 220 (2019).
- [35] Y. Sun, R. Wang, and K. Liu, *Appl. Phys. Rev.* **4**, 011301 (2017).
- [36] G. Froehlicher, E. Lorchat, and S. Berciaud, *Phys. Rev. X* **8**, 011007 (2018).
- [37] K. V. Emtsev, A. Bostwick, K. Horn, J. Jobst, G. L. Kellogg, L. Ley, J. L. McChesney, T. Ohta, S. A. Reshanov, J. Röhrli,

- E. Rotenberg, A. K. Schmid, D. Waldmann, H. B. Weber, and Th. Seyller, *Nat. Mater.* **8**, 203 (2009).
- [38] S. Forti and U. Starke, *J. Phys. D* **47**, 094013 (2014).
- [39] C. Riedl, C. Coletti, and U. Starke, *J. Phys. D* **43**, 374009 (2010).
- [40] A. Mohammed, H. Nakamura, P. Wochner, S. Ibrahimkuty, A. Schulz, K. Müller, U. Starke, B. Stuhlhofer, G. Cristiani, G. Logvenov, and H. Takagi, *Appl. Phys. Lett.* **111**, 073101 (2017).
- [41] C. Nicklin, T. Arnold, J. Rawle, and A. Warne, *J. Synchrotron Rad.* **23**, 1245 (2016).
- [42] See Supplemental Material at <http://link.aps.org/supplemental/10.1103/PhysRevB.101.165103> for details on ARPES EDC fitting to derive the spin splitting, the lattice constant determination in GIXRD, and additional first-principles calculations with the relaxed lattice (see also Refs. [51–53] therein).
- [43] P. Blaha, K. Schwarz, G. K. H. Madsen, D. Kvasnicka, and J. Luitz, *WIEN2k: An Augmented Plane Wave + Local Orbitals Program for Calculating Crystal Properties* (Karlheinz Schwarz, Technische Universität Wien, Vienna, 2001).
- [44] G. te Velde and E. J. Baerends, *Phys. Rev. B* **44**, 7888 (1991).
- [45] BAND 2019.3, SCM, Theoretical Chemistry, Vrije Universiteit, Amsterdam, the Netherlands, <http://www.scm.com>.
- [46] J. P. Perdew, K. Burke, and M. Ernzerhof, *Phys. Rev. Lett.* **77**, 3865 (1996).
- [47] W. J. Schutte, J. L. De Boer, and F. Jellinek, *J. Solid State Chem.* **70**, 207 (1987).
- [48] J. Ristein, S. Mammadov, and Th. Seyller, *Phys. Rev. Lett.* **108**, 246104 (2012).
- [49] S. Mammadov, J. Ristein, J. Krone, C. Raidel, M. Wanke, V. Wiesmann, F. Speck, and Th. Seyller, *2D Mater.* **4**, 015043 (2017).
- [50] J. Sforzini, L. Nemeč, T. Denig, B. Stadtmüller, T.-L. Lee, C. Kumpf, S. Soubatch, U. Starke, P. Rinke, V. Blum, F. C. Bocquet, and F. S. Tautz, *Phys. Rev. Lett.* **114**, 106804 (2015).
- [51] A. J. C. Wilson, *Acta Crystallogr.* **23**, 888 (1967).
- [52] J. Hass, R. Feng, J. E. Millán-Otoya, X. Li, M. Sprinkle, P. N. First, W. A. de Heer, E. H. Conrad, and C. Berger, *Phys. Rev. B* **75**, 214109 (2007).
- [53] E. S. Kadantsev, R. Klooster, P. L. de Boeij, and T. Ziegler, *Mol. Phys.* **105**, 2583 (2007).